RESEARCH

Study of Thermodynamic, Optoelectronic and Thermoelectric Properties of BaSiO$_3$ Crystals Doped With Er^{3+} and Yb^{3+} for Energy Renewable Devices Applications

Madiha Khalid[1] · Sikander Azam[1] · Muhammad Tahir Khan[2,3] · Qaiser Rafiq[4] · Adil Mehmood[1] · Mohammad Altaf[5] · Wilayat Khan[6]

Abstract

The optoelectronic properties of doped BaSiO$_3$-based semiconductors play a very significant role in modern optoelectronic devices. We provide key insights into their versatility and potential in developing technologies by analyzing their structural, electrical, elastic, optical and thermoelectric properties using Wien2k software and GGA + U method. The aim of this research is to enhance the usability of complex resources for new and practical applications. We begin our analysis by applying Birch-Murnaghan fitting to study the structural features of BaSiO$_3$ crystals doped with Er^{3+} and Yb^{3+}. This study explores the structural, electronic, and thermoelectric enhancements of BaSiO$_3$ semiconductors doped with Er^{3+} and Yb^{3+}. Through detailed analysis, we have identified critical modifications in the lattice parameters and crystal structures, confirming an improvement in general stability and functionality. Notably, doping has effectively reduced the energy band gap from 1.12 eV in undoped BaSiO$_3$ to a metallic state, optimizing the material for optoelectronic applications. The introduction of Er^{3+} significantly increases optical absorption and reduces the optical band gap, while Yb^{3+} extends absorption into the near-infrared spectrum. Both dopants particularly enhance the thermoelectric properties of BaSiO$_3$, with a marked increase in the power factor. Additionally, these doped materials show substantial absorption of ultraviolet photons and moderate reflection across infrared and visible spectra. The findings from this research position Er^{3+} and Yb^{3+} doped BaSiO$_3$ as promising materials for advanced thermoelectric and optoelectronic applications, suggesting potential for significant technological advancements in energy-efficient devices.

Keywords Optoelectronic Properties · Thermoelectric Properties · Renewable Devices Applications

✉ Sikander Azam
sikander.physicst@gmail.com

✉ Muhammad Tahir Khan
sikander.physicst@gmail.com

1 Department of Physics, Riphah International University, Islamabad 44000, Pakistan

2 Key Laboratory of Urban Rail Transit Intelligent Operation and Maintenance Technology and Equipment of Zhejiang Province, College of Engineering, Zhejiang Normal University, Jinhua, Republic of China

3 School of Computer Science and Technology, Zhejiang Normal University, Jinhua, Republic of China

4 Department of Physics, International Islamic University, Islamabad, Pakistan

5 Department of Chemistry, College of Science, King Saud University, P.O. Box 2455, 11451 Riyadh, Saudi Arabia

6 Department of Physics, Bacha Khan University, Charsadda, Pakistan

1 Introduction

The increasing demand for clean energy has significantly spurred research into developing efficient and cost-effective energy conversion materials. Among the many materials studied for energy conversion applications, inorganic crystalline materials have attracted significant attention due to their distinctive and adjustable optoelectronic and thermoelectric properties [1–3]. BaSiO$_3$, in particular, is an important inorganic material that has received considerable attention for its potential in a range of applications, including optoelectronics, photovoltaics, and thermoelectrics. The interest in BaSiO$_3$ is attributed to its wide bandgap, high dielectric function, and low phonon energy, which makes it an ideal candidate for energy conversion applications [4].

Enhancing the performance of BaSiO$_3$ for energy conversion applications can be significantly achieved by doping

with rare earth elements such as Erbium (Er^{3+}) and Ytterbium (Yb^{3+}) [5, 6]. These elements alter the electronic and optical properties of the host material, thus improving its functionality in energy conversion settings. Due to their distinctive optical and electronic characteristics, Erbium and Ytterbium have garnered extensive interest as dopants. Specifically, Erbium is renowned for its robust absorption and emission within the visible and near-infrared spectra, while Ytterbium is notable for its high absorption coefficient in the near-infrared range [7–10].

Extensive research, including studies by Wang et al. and Kumar et al., have validated the synthesis and enhanced luminescence properties of Erbium and Ytterbium-doped $BaSiO_3$ crystals under varying dopant concentrations and synthesis conditions. These studies have illustrated the potential to fine-tune the material's electronic and optical properties, which is crucial for optimizing their application in energy conversion technologies [11, 12].

Despite existing research, there remains a gap in comprehensive analysis concerning how varying concentrations of dopants and different synthesis conditions affect the overall performance of $BaSiO_3$ crystals. This study aims to fill this gap by exploring the optoelectronic and thermoelectric properties of $BaSiO_3$ crystals doped with Erbium and Ytterbium, employing advanced simulation techniques such as Wien2k and GGA + U methods. Our objectives are to unravel the fundamental mechanisms that underpin the enhanced performance of these doped crystals and to identify key parameters that could be optimized to further improve their efficiency and effectiveness in energy conversion applications. This research is poised to contribute significantly to the development of next-generation materials for sustainable energy solutions.

This study was motivated by the need to improve the efficiency and functionality of $BaSiO_3$-based semiconductors in renewable energy devices. Despite significant advancements in material science, the full potential of $BaSiO_3$ in optoelectronic applications has not been fully realized due to limitations in understanding and optimizing its doped properties. Our research aims to fill these gaps by providing detailed insights into the optoelectronic and thermoelectric properties of $BaSiO_3$ doped with Er^{3+} and Yb^{3+}, thus paving the way for more efficient and cost-effective energy conversion materials.

2 Computational Method

The computational study of $BaSiO_3$ crystals doped with Er^{3+} and Yb^{3+} (see crystal structures in Fig. 1) was carried out using the WIEN2K code [13] and the full potential linear augmented plane wave (FP-LAPW) methods, based on density-functional theory (DFT) [14–16]. For handling
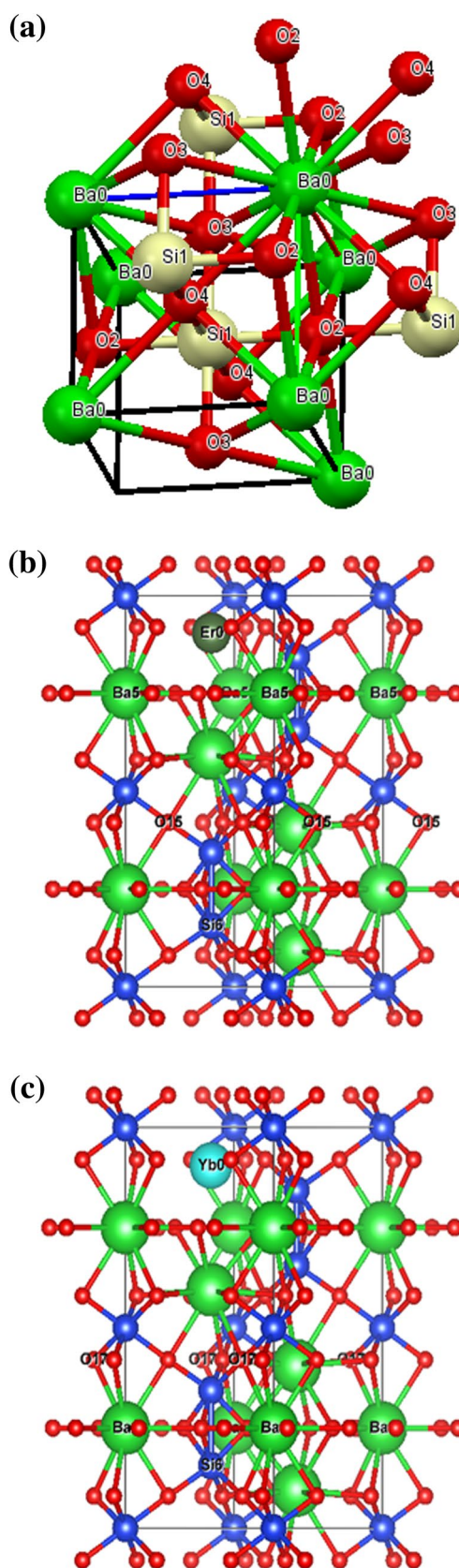
Fig. 1 Visualization of cubic primitive crystalline unit cell of **a** $BaSiO_3$, **b** $BaSiO_3$:Er^{3+}, and **c** $BaSiO_3$:Yb^{3+} compounds

the exchange–correlation functional in order to provide favorable magnetic characteristics, we use the generalized gradient approximation GGA [14], as well as the GGA + U [17], where U is on-site Coulomb interaction correction. We employed the GGA + U to accurately forecast optoelectronic properties because GGA does not correctly treat optoelectronic properties of materials with significant electronic correlation. As a result, Hubbard's adjustment was applied to compensate for effective Coulomb interaction parameters between Er and Yb atoms' coupled electrons. These findings show that the GGA + U formalism may be used to investigate the band structure as well as optoelectronic properties of a wide range of materials with significant electronic correlation. The supercell size of $2 \times 2x2$, utilized in our simulations to model the doped $BaSiO_3$ system, provides an optimal balance between computational efficiency and the detailed representation required to accurately assess the material's electronic and optical properties. This choice ensures precise simulation results while managing computational resources effectively.

In our computational approach, the self-consistent field (SCF) cycles were carefully monitored to ensure accuracy and stability of the results. The energy convergence threshold was set at 10^4 Ry per formula unit, which is a stringent criterion that aids in achieving precise and reliable outcomes. This setting was crucial for ensuring that the electronic structure calculations were thoroughly converged, providing a robust basis for our analysis. We have adjusted the initial recommendations in this study to R_{MX} $K_{max} = 8.0$, where R_{mt} is the smallest atomic sphere radius and K_{max} is the highest value of the biggest K vector in the plane wave expansion, and the angular momentum vector is kept at $l_{max} = 10$. To execute integration over the first Brillouin zone BZ, the complete Brillouin zone is sampled with 1000 k-points. When the self-consistent calculation reaches 10^4 Ry per formula unit, it is said to have reached energy convergence. The Er-$4f^{12}$ orbital transition metal is closely associated with different U values (where U = 0, 3, 4, 5, 6, 7, 8 and 9 eV) in this computation. Where we found stable values on 7 eV.

Figure 1a illustrates the crystal structure of a $BaO-SiO_2$ compound, highlighting the arrangement of Ba (green spheres) and Si (blue spheres) atoms, interconnected by O (red spheres). The structure provides insights into the lattice framework and potential interaction points for electronic properties. Figure 1b Depicted here is the doped crystal structure of $BaO-SiO_2$, where Er (light blue sphere) is introduced into the matrix. The incorporation of Er atoms demonstrates the modification in the crystal lattice, which may influence the optical and electrical properties of the material. Figure 1c shows the Yb-doped $BaO-SiO_2$ crystal structure, with Yb (light blue sphere) atoms integrated within the lattice. Yb doping is known to affect the material's dielectric

and magnetic properties, making this visualization crucial for understanding the structural changes.

3 Results and Discussion

An extensive analysis of a material's mechanical, electrical, and optical properties is necessary before it can be used in a variety of applications. These characteristics work together to determine the material's suitability for a variety of uses, including energy conversion systems and structural parts in engineering and electronics.

3.1 Structural properties

We used an optimization approach, which minimizes the total energy, to thoroughly analyze the lattice parameters for the compounds $BaSiO_3$, $BaSiO_3:Er^{3+}$, and $BaSiO_3:Yb^{3+}$. In order to perform this optimization, the unit cell capacity was changed, and the total energy was tracked in relation to these variations. Figure 2 presents the data that illustrates the correlation between energy and volume. We used a fitting method based on the Murnaghan equation of state to extract important ground-state properties of these compounds, including important parameters like the lattice constant (a_0), bulk modulus (B_0), pressure derivatives of the bulk modulus (B_0'), equilibrium volume (V_0) at zero pressure, energy gap (E_g) in electron volts (eV), and ground-state energy (E_0) in Rydberg (Ry) [18].

$$E_{tot}(V) = E_o(V) + \frac{B_o(V)}{B_o\prime(B_o\prime - 1)}[B\left(1 - \frac{V_o}{V}\right) + \left(\frac{V_o}{V}\right)^{B_o\prime} - 1]$$

where $E_{tot}(V)$, V, B_o and $B_o\prime$ is the total energy as a function of volume bulk modulus and the last one represent the pressure derivative of bulk modulus, where V_0 is the reference volume.

Table 1 provides the comprehensive numerical findings for these features. This table provides a thorough reference for the basic characteristics of the compounds that have been optimized. In particular, Table 1, indicates the lattice parameters for $BaSiO_3$, $BaSiO_3:Er^{3+}$, and $BaSiO_3:Yb^{3+}$ according to our findings. In order to investigate the concept of material hardness, the bulk modulus (B), which measures a material's resistance to compression, might be taken into consideration. Greater hardness is essentially indicated by a higher bulk modulus, which suggests that the material is less likely to compress or deform under pressure.

A 40 GPa threshold is frequently applied as a criterion when discussing hardness [19, 20]. Bulk moduli greater than this are usually classified as very hard, which shows low compressibility and hard crystalline formations. For $BaSiO_3$, $BaSiO_3:Er^{3+}$, and $BaSiO_3:Yb^{3+}$, the computed
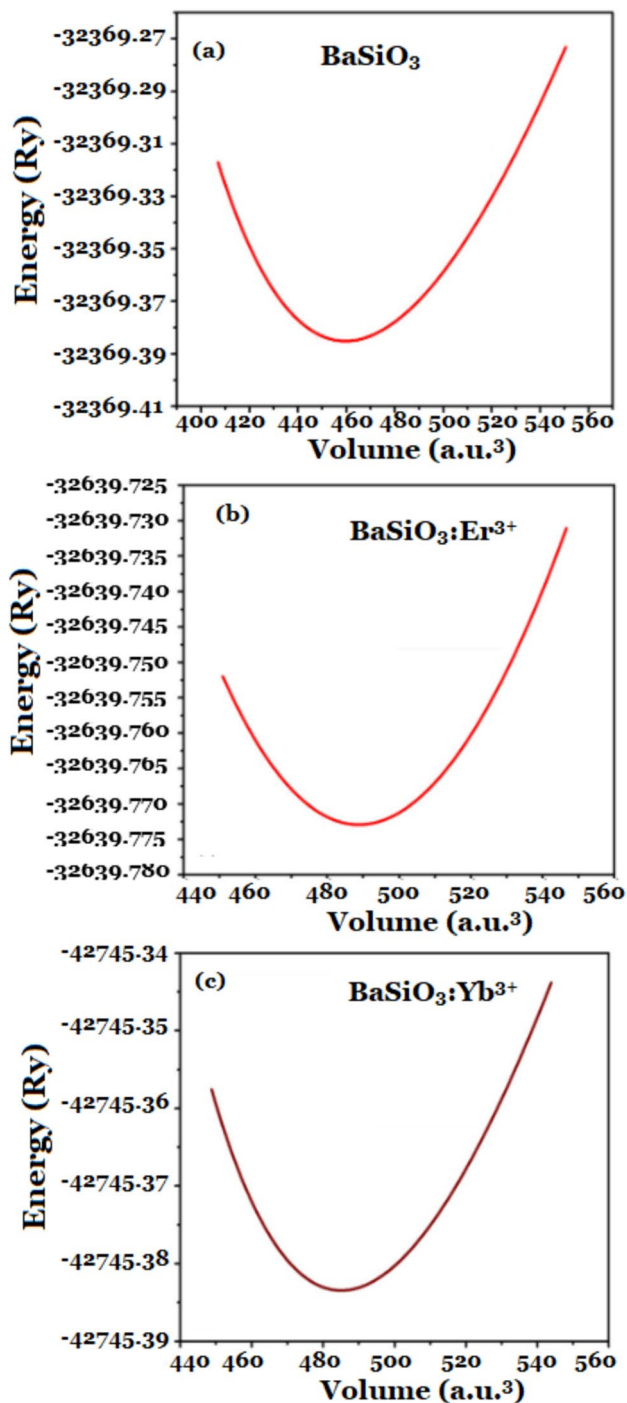
Fig. 2 Structural optimization curve for **a** BaSiO$_3$ using GGA **b** BaSiO$_3$:Er^{3+}, and **c** BaSiO$_3$:Yb^{3+} using GGA + U

bulk modulus values (B$_0$) were 180.56, 169.13, and 188.10 GPa, respectively. These findings show that BaSiO$_3$ and BaSiO$_3$:Er^{3+} is less prone to deformation and compression than BaSiO$_3$:Yb^{3+} because it has a much higher degree of hardness and stiffness. Understanding these materials' mechanical characteristics is important because it affects

how well they work in different applications, especially ones that call for materials with high stiffness and hardness levels.

3.2 Band structure

We used the PBE-GGA and GGA + U approximations to calculate the spin-polarized electronic band structure along with the density of states of the Er/Yb-doped BaSiO$_3$ compound at its stability lattice parameters in this study. The band structures of the BaSiO$_3$ compound along the high symmetry directions of the first Brillouin zone are shown in Fig. 3 for the GGA approximation, Figs. 4, and 5 for the GGA + U respectively. The energy bands in the valence band cut the Fermi level in minority -spin states (spin-down case), but they are placed bottom the Fermi level in majority -spin states (spin-up case), proving the complete half-metallic characteristic of this compound.

3.3 Density of States

To compute various optical properties and the distribution of electrons and holes within a material, we need to know the density of states. The density of states (DOS) is defined as the number of available electronic states per unit energy per unit volume. The contribution of various electronic states in the valance and conduction bands determines the electronic band structure of semiconducting materials. The density of states accurately explains the contributions of various electronic states in the valence /conduction band [21]. We can use the density of states to investigate electronics and their particular atomic and orbital origins. We estimated the total as well as partial density of states for BaSiO$_3$ doped with Er and Yb materials with GGA, and GGA + U as shown in Figs. 6 and 7a, b and c.

In Fig. 3.1, the TDOS and PDOS of BaSiO$_3$ with Er—doped in the energy range of E$_f$ -12 eV to E$_f$ -10 eV are computed. E$_f$ stands for fermi level. The valance band is shown to the left of E$_f$, whereas the conduction band is shown to the right of E$_f$.

This image clearly illustrates that the TDOS is about the same in both spins (Up and Down), confirming the material's semiconductor nature. The bandgap between the valence and conduction bands is about 2.9 eV. The PDOS plot is shown in Fig. 7a-c. In the energy range of (-13 eV to-11 eV), Ba-p states dominate the lower valance band, whilst O-p states dominate the top valance band. A peak of Er-*s* can also be seen in the valance band, which is at-6.4 eV. The conduction band minimum is primarily made up of Er-s and Er-*f* states, whereas the conduction band maximum is primarily made up of Er-*d* and Ba-*d* states, with minor contributions from Ba-*p* states.

Table 1 Estimated parameters, lattice constants (a_0), Bulk moduli, (B), pressure derivative of bulk modulus B′, ground state volume (V_0) and ground state energy (E_0), for $BaSiO_3$, $BaSiO_3:Er^{3+}$, and $BaSiO_3:Yb^{3+}$ compounds

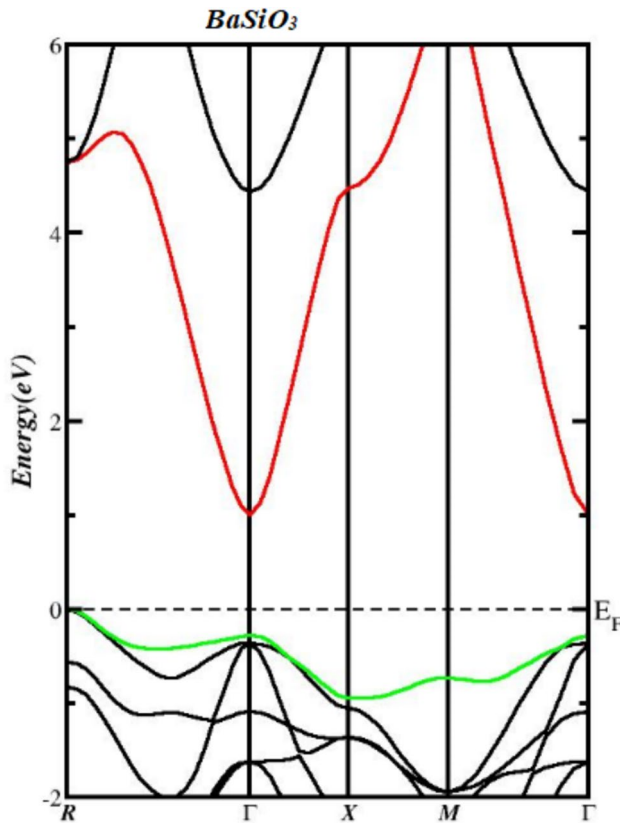|	Experimental	$BaSiO_3$ This work	$BaSiO_3:Er^{3+}$ This work	$BaSiO_3:Yb^{3+}$ This work
parameter/method		GGA	GGA + U	GGA + U
lattice constant a_0 (Å)	a = 5.518273 c = 13.280251	a = 5.4354996 c = 13.0810472	a = 5.407908 c = 13.014646	a = 5.418945 c = 13.280251
equilibrium volume V_0 (Å^3)		63.71	63.33	63.10
bulk modulus B_0 (GPa)		169.13	188.10	176.38
first pressure derivative B_0'		4.75	5.52	5.97

Fig. 3 Band structure of $BaSiO_3$ using GGA

Figure 8 shows the TDOS and PDOS of Yb doped $BaSiO_3$ in the energy range of -15 eV to 8 eV. According to the TDOS graph, the energy band gap is around 3.9 eV.

There will be some overlapping at the Fermi Energy level, which shows the metallic nature of the material. Figure 7a, b shows PDOS graphs in which Ba-*p* states dominate the lower valence band in the energy range of (14.8 → -12.3 eV) O-p states contribute minimally in the energy range of (-12 eV→ -4 eV) and Ba-*s* states dominate the upper valence band. The conduction band minimum is majorly composed of Ba-*s* states along with Yb-*f* states and also Yb-*s* and Ba-*p* states contributed minutely, while the conduction band maximum is contributed mainly by Yb-*s* states along with the contribution of Ba-*p* states, and Yb-*f* states also contributed minutely.

3.4 Optical Properties:

Optical properties are significant to determine photovoltaic device efficiency and explore their viability for solar applications. The optical features of solid are computed using interactions of incoming photons by electrons in compounds. The majority of energy-dependent optical features are determined by the material's electronic band structure. The electronic density of states for different energies above and below the Fermi level is determined by this band structure, so these states are implicated for photon-induced electrical transformations. This section contains, the dielectric function, optical absorption coefficient, refractive index, reflectivity, optical conductivity, and energy loss function of Er and Yb doped $BaSiO_3$ are computed with various incident photon energies using the FP-LAPW + lo method. A material's optical response at all photon energies can be represented by a complex dielectric function ε(ω).

3.4.1 The Dielectric Functions ε″(ω):

An important parameter to address the optical properties is the calculation of the dielectric function "ε(ω)" which discusses light-matter interaction. This parameter can be divided into real "ε′(ω)" and imaginary ε″(ω) components obtained from Kramer-Kronig relations as explained previously [22]. The dielectric functions of metallic materials consist of intraband as well as interband transitions. Intra band transitions, on the other hand, contribute very little to the dielectric function in semiconducting systems. As a result, we've only included interband transitions in our computations so far. Because of its little contribution to ε(ω), the indirect interband transition can be ignored when compared to the direct interband transition [23]. Dielectric function ε(ω), is used to compute optical properties also calculated in the following way [24, 25]:

$$\varepsilon(\omega) = \varepsilon'(\omega) + i\varepsilon''(\omega) \qquad (1)$$

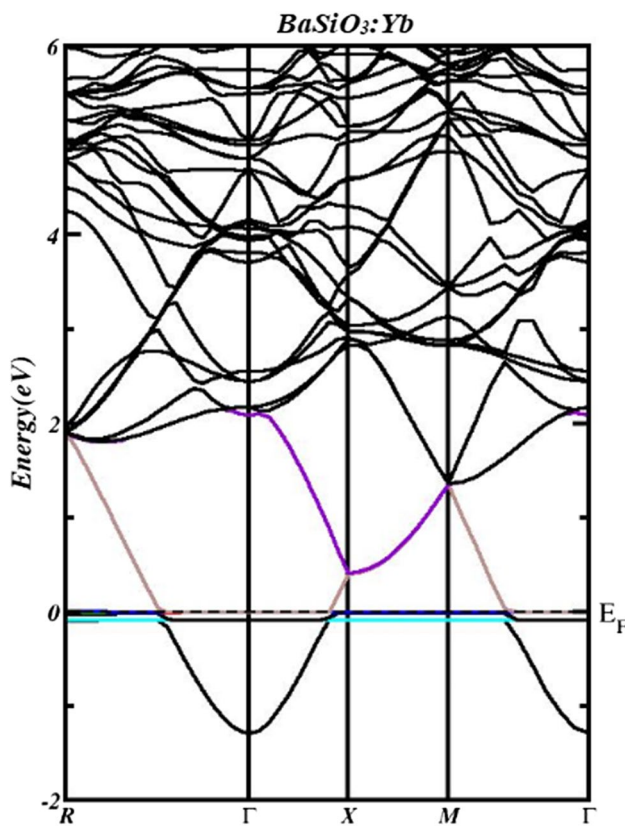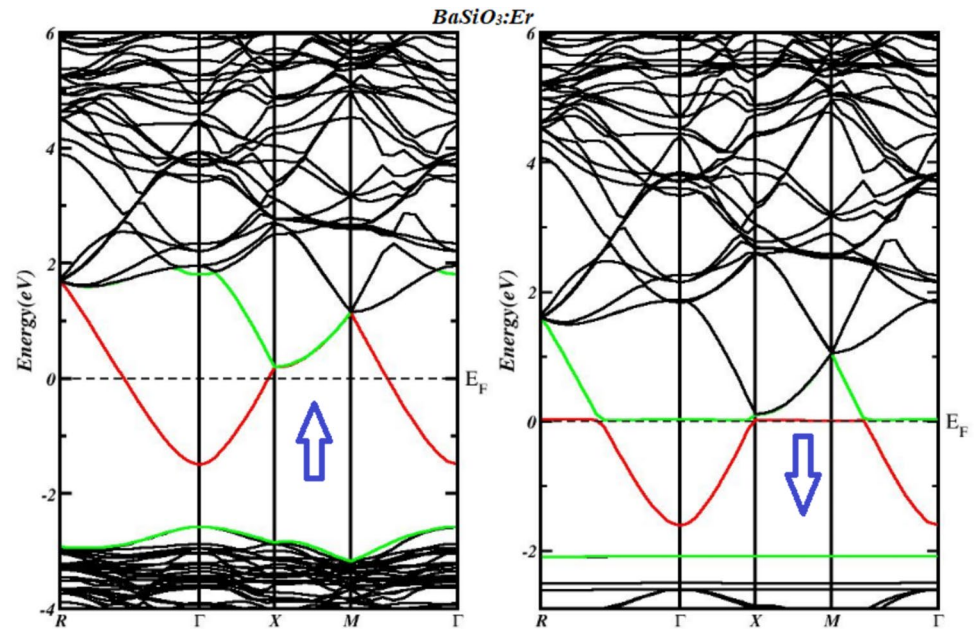**Fig. 4** Band structure of BaSiO₃: Er for spin up ↑ and spin down ↓ using GGA+U

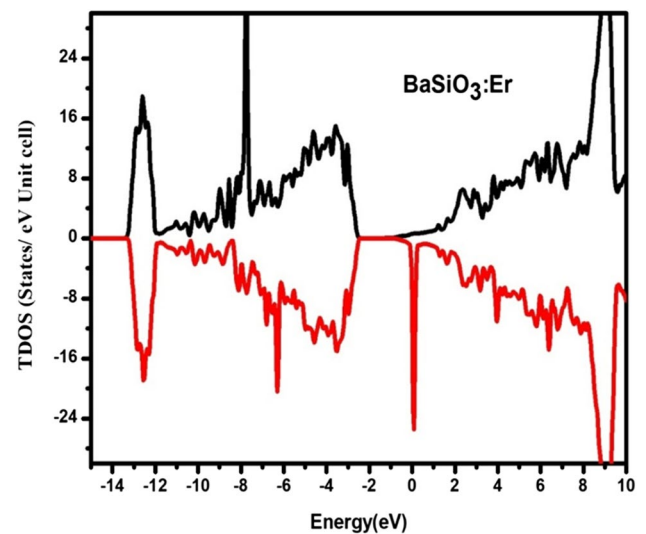**Fig. 5** Band structure of BaSiO₃: Yb using GGA

Fig. 6 The Calculated TDOS of Er-doped BaSiO₃

To compute the imaginary component of the complex dielectric function $\varepsilon''(\omega)$, use the following formula. [26]:

$$\varepsilon''(\omega) = \frac{4\pi\ e^2}{m^2\omega^2} \sum_{ij} \int \langle iMj \rangle^2 F_i (1 - F_j) \delta(E_{j,k} - E_{i,k} - \omega) d^3k$$

(2)

ω is the photon energy, M is the dipolar matrix element, e is the charge of an electron, m is the mass of an electron, and $F_{i(j)}$ is the Fermi distribution function of $i^{th}(j^{th})$ electronic state. $E_{i,k}$ and $E_{j,k}$ represents electron energies of ith and j^{th} levels. The energy is conserved using the delta function. By
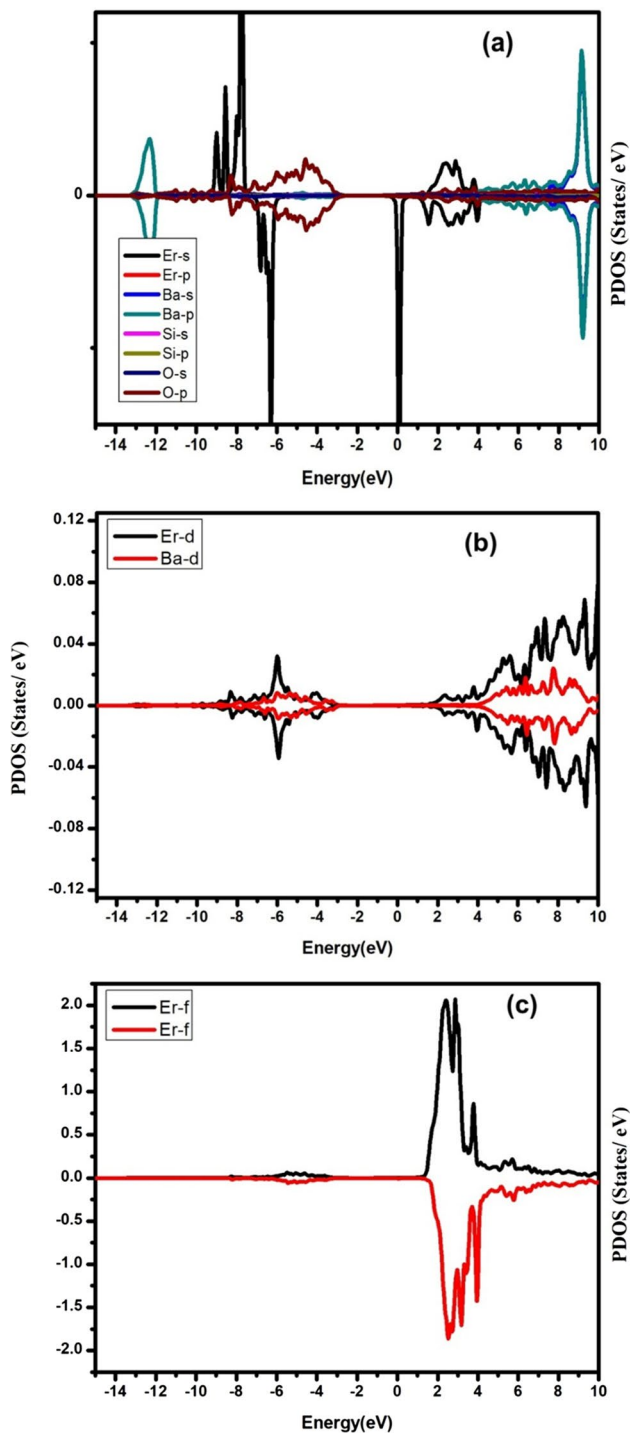
Fig. 8 The Calculated TDOS of Yb doped $BaSiO_3$. **a**, **b** The Calculated PDOS of Yb doped $BaSiO_3$

$$\varepsilon'(\omega) = 1 + \frac{2}{\pi} \int_0^\infty \frac{\omega \varepsilon''(\omega) d\,\omega}{\omega'^2 - \omega^2} \tag{3}$$

The real or imaginary parts of $\varepsilon(\omega)$ could be used to extract various terms, like absorption coefficient $\alpha(\omega)$, refractive indexes $n(\omega)$, conductivity $\sigma(\omega)$, reflectivity $R(\omega)$, or energy loss $L(\omega)$ [28]:

$$n(\omega) = \frac{1}{\sqrt{2}} \left(\left[\varepsilon'(\omega) + \sqrt{\varepsilon'(\omega)^2 + \varepsilon''(\omega)^2} \right]^{\frac{1}{2}} \right) \tag{4}$$

$$\alpha(\omega) = \sqrt{2\omega} \left(\left[\sqrt{\varepsilon'(\omega)^2 + \varepsilon''(\omega)^2} - \varepsilon'(\omega) \right]^{\frac{1}{2}} \right) \tag{5}$$

$$\sigma(\omega) = \frac{-i\omega}{4\pi} \varepsilon(\omega) \tag{6}$$

$$R(\omega) = \frac{\left| \sqrt{\varepsilon(\omega) - 1} \right|}{\left| \sqrt{\varepsilon(\omega) + 1} \right|^2} \tag{7}$$

$$L(\omega) = \frac{\varepsilon''(\omega)}{\varepsilon'^2 + \varepsilon''^2} \tag{8}$$

Figures 9 and 10 show changes in imaginary & real parts of a complex dielectric function of Er and Yb doped $BaSiO_3$ with the energy of an incident photon. The real part $\varepsilon'(\omega)$ depicts light dispersion as it interacts with host lattice, whereas the imaginary part $\varepsilon''(\omega)$ depicts absorption of light because of interband electronic transformations.

Fig. 7 **a**, **b**, **c** The Calculated PDOS of Er-doped $BaSiO_3$

using Kramers–Kronig transition, the real part of a complex dielectric function, $\varepsilon'(\omega)$ could be derived using the imaginary part of a complex dielectric function, $\varepsilon''(\omega)$, by following equation [26, 27]:
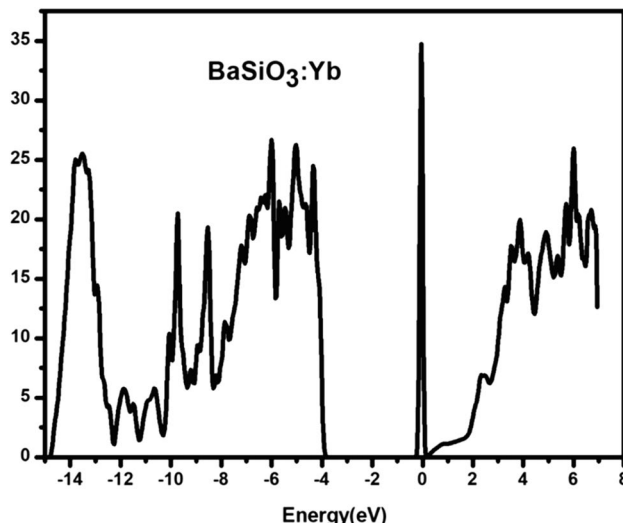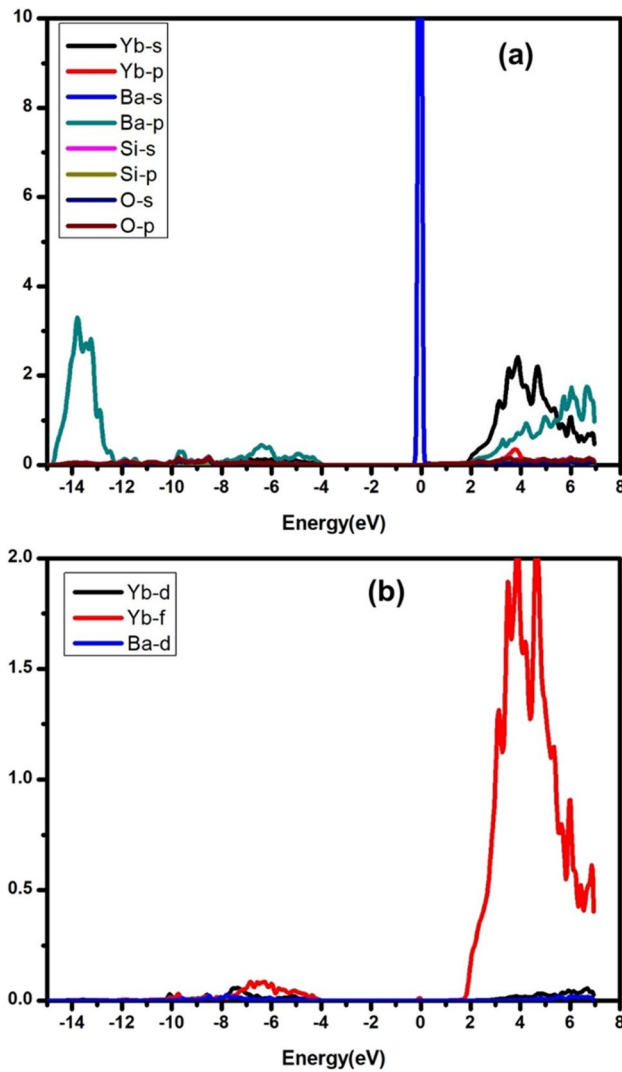
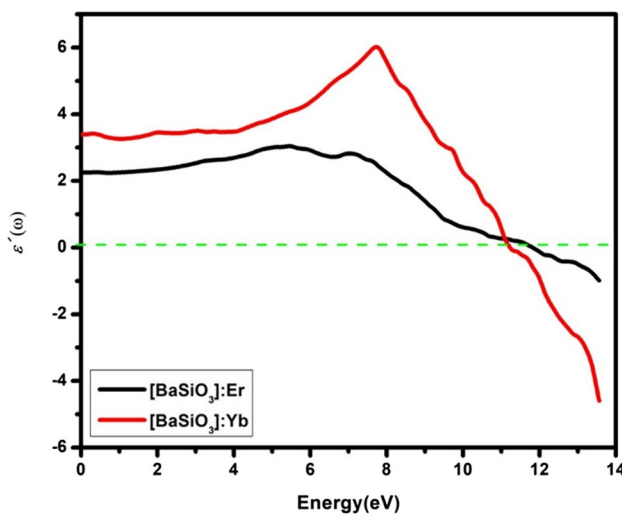**Fig. 9** Calculated Real part of dielectric function

Fig. 10 Calculated Imaginary part of dielectric function

The Penn model may explain the static value of the dielectric function $\varepsilon'(0)$, which significantly connected with the bandgap (inverse relationship with bandgap) [29, 30], and is given by the relation;

$$\varepsilon(0) = \varepsilon'(0) \approx 1 + \left(\frac{\hbar\omega_p}{E_g} \right)^2 \tag{9}$$

Equation (9) represents the static value of the real part of the dielectric function, $\varepsilon'(0)$, which is crucial for understanding the optical properties of materials. In this equation, $\hbar\omega_p$ is the plasma energy, where $\hbar$ is the reduced Planck constant and ω_p is the plasma frequency, representing the collective oscillations of the free charge carriers within the material. E_g is the energy band gap of the material, indicating the minimum energy that electrons require to transition from the valence band to the conduction band. The equation approximates $\varepsilon'(0)$ as being directly influenced by the ratio of the plasma energy squared to the square of the energy band gap, illustrating how the electronic properties of the material affect its optical response. This relation is crucial for evaluating the optical performance and electronic structure of the doped BaSiO₃ crystals.

In current work, the dielectric function's static value is 3.5 for Er-doped $BaSiO_3$ and 2.3 for Yb doped $BaSiO_3$. As can be seen in Fig. 3.3, $\varepsilon'(\omega)$ increases gradually with increasing energy to reach a maximum value of about 8 eV for Er-doped $BaSiO_3$ and 7 eV for Yb doped $BaSiO_3$, then decreases faintly by increasing energy, reaching zero-cross value on 11.3 eV for Er-doped $BaSiO_3$ and 12 eV for Yb doped $BaSiO_3$, this correlates to Plasmon Resonance. Beyond these energies, it exhibits a negative sign within (11.5 eV to 14 eV), which shows that no wave would propagate farther. This negative $\varepsilon'(\omega)$ illustrates $BaSiO_3$ metals-like nature. The modest change of $\varepsilon'(\omega)$ spectrum towards high energy & bandgap modification in ultraviolet energy range shows the significance of $BaSiO_3$ used for optoelectronic application.

The Imaginary part of a dielectric function $\varepsilon''(\omega)$, which is shown in figure 3.4, depicts an optical transformation method. The Imaginary part of a complex dielectric function among unoccupied or occupied states among conduction or valence band (interband transitions), electronic states can be used to identify possible electronic transitions. In line with magnitude and peak positions in TDOS centered on the Fermi level, the imaginary component of a dielectric function rises and shows peaks. The incoming energy absorbed by $BaSiO_3$ is expressed by $\varepsilon''(\omega)$. The critical value of $\varepsilon''(\omega)$ is a one-of-kind characteristic that indicates threshold energy below & above which $BaSiO_3$ exhibits transmission or absorption, respectively.

Photon absorption occurs only when the photon energy is high enough to stimulate the transition of electrons from the

valance band maximum to the conduction band minimum. For Er-doped $BaSiO_3$, it is clear that until 2.9 eV, $\varepsilon''(\omega)$ is zero, after that it climbs to its highest value in the UV range (peak about 9 eV), and then gradually decreases as photon energy increases. For Yb doped $BaSiO_3$ it is clear that until 3.7 eV, $\varepsilon''(\omega)$ is slightly increasing, after that, it climbs to its highest value in the UV range (peaks about 9.7 eV also 11 eV) and then gradually decreases as photon energy increases. From the graph, it is seen that maximum absorption is in the UV region.

3.4.2 Absorption Co-efficient α(ω):

When deciding whether a material is acceptable for solar cell applications, the absorption coefficient $\alpha(\omega)$ is significant. The amount of light absorbed by a specific substance is measured by this coefficient. This parameter explains the possible electronic transformation of electrons from VB to CB upon receiving photon energy. The spectrum of absorption coefficient can reveal information about a semiconducting material's optical absorption range, revealing potential uses of the material in optoelectronic devices. The spectrum of optical absorption coefficient derived using the GGA + U formalism for Er and Yb doped $BaSiO_3$ is given in Fig. 11. The absorption coefficient's magnitude is determined by the geometry of the electronic band structure and matrix element of electronic transitions.

Absorption coefficient $\alpha(\omega)$ is strongly connected with $\varepsilon''(\omega)$ and describes the quantity of incident light attenuated by compound or subsequent decay of this light roaming through absorbing medium [31].

Absorption coefficient begins to rise at photon energies greater than 4.0 eV for Er-doped $BaSiO_3$ and 4.5 eV for Yb doped $BaSiO_3$, and then peaks at 13.5 eV and 13.3 eV for
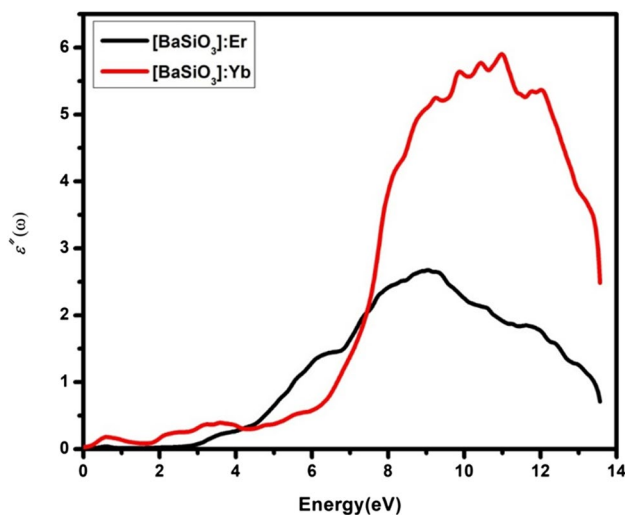
Er-doped $BaSiO_3$ and Yb doped $BaSiO_3$ respectively. This maximum value arises due to the interband transitions from the bonding band to the anti-bonding band respectively. It shows that these modified materials could be used as promising materials to optoelectronic devices operating through the UV area because of their extraordinarily strong cut-off response, especially in such energy regions. Figure 3.5 also shows that throughout the entire visible region $\alpha(\omega)$ is negligible, after which it steadily increases, which shows that these doped materials are optically translucent in this region. This is simple to understand that when visible light is incident on these doped materials, they do not absorb any of it and the entire part of the light passes through them. This opens up a lot of possibilities for using these materials as a hole transport layer in solar cells. It will improve the solar cell's efficiency by allowing all incident solar light to be absorbed [32, 33]. The increase in absorption trends for $BaSiO_3$ crystals doped with Er^{3+} and Yb^{3+} is primarily due to the doping-induced reduction in the energy band gap. Er^{3+} enhances optical absorption by modifying the crystal lattice and lowering the optical band gap, allowing for transitions at lower energies. Simultaneously, Yb^{3+} doping extends absorption into the near-infrared spectrum, broadening the material's responsiveness across various wavelengths. These changes optimize the material for improved optoelectronic applications.

3.4.3 Refractive Index n(ω):

Electromagnetic waves' behavior in solid materials is extensively described by $n(\omega)$. The bending of light as it passes obliquely through a substance is measured by $n(\omega)$. A high refractive index corresponds to the narrow bandgap and vice versa. If $n(\omega)$ is close to zero, the material is transparent, but positive values indicate light absorption. When a photon is incident on the lattice, the refractive index $n(\omega)$ analyses the type of interactions that occur and describes the bonding types in material [34]. For strong interactions of shared electrons with incoming photons to reduce their energy, covalently bound materials have a higher $n(\omega)$ value than ionic compounds. The degree to which a material is transparent can be explained by $n(\omega)$, with semiconductors ranging from 2–3 [35]. Figure 12 illustrates a broad range graph of $n(\omega)$ for both modified systems, demonstrating that, $n(\omega)$ spectrum approximately follows the real part of $\varepsilon'(\omega)$ graph, this demonstrates that such doped systems maintain a positive value of $n(\omega)$, which characterizes both the behavior of incident light as it interacts with the material and the general extent of light refraction.

Static value of $n(\omega)$ for Yb doped $BaSiO_3$ is 1.82. This number continues to rise, throughout the visible region, reaching its maximum value of 2.45 at 7.9 eV lying in the UV region. With increasing energy, $n(\omega)$ decreases, which
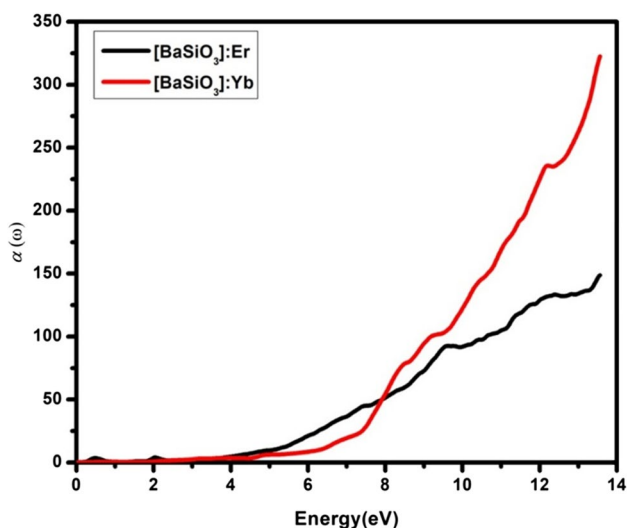

Fig. 11 Calculated Optical Absorption Coefficient

Fig. 12 Calculated Refractive Index

Fig. 13 Calculated Optical Energy Loss

shows that incident light's emerging photons have fewer interactions with materials. As they are both interconnected by statement $n(0) = \sqrt{\varepsilon'(0)}$, the tendency of fluctuation of $n(\omega)$ matches almost identically with that of the $\varepsilon'(\omega)$ spectrum [31]. Also, the static refractive index of Er-doped $BaSiO_3$ is 2.0. The first small peak of $n(\omega)$ is observed at 0.4 eV having a value of 2.1 and then suddenly decreases to 1.25 at 0.6 eV. After this energy, the value of $n(\omega)$ starts increasing and reaches its maximum value of 1.75 at 5.6 eV lying in the UV region.

At energy points of 11.8 eV for Er-doped $BaSiO_3$ and 13.5 eV for Yb doped $BaSiO_3$, $n(\omega)$ touches unity. $n(\omega)$ falls below unity above these energies. This shows that group velocity V_g of the incident light is larger than the speed of light in a vacuum, causes V_g to move to the negative domain and the nature of the medium shifts from linear to non-linear, enabling that material to be superluminal in UV range [36, 37]. In other words, for high-energy photons, the material becomes superluminal. The higher value of $n(\omega)$ is positioned in the UV region, confirms that the current material has higher optical absorption of UV light.

3.4.4 Energy Loss Function $L(\omega)$:

This spectrum explains the electrons' energy loss in material or compound as they pass quickly through the medium due to incident photon energy. $L(\omega)$ reflects the likely interactions of fast-moving electrons with a material, which occur as a result of interband transitions, inner-shell ionization, phonon excitations, and plasmon excitations [38].

When electromagnetic radiation interacts with a material, its free conduction electrons are stimulated, allowing us to identify plasmonic excitations. Peaks of $L(\omega)$ relate with
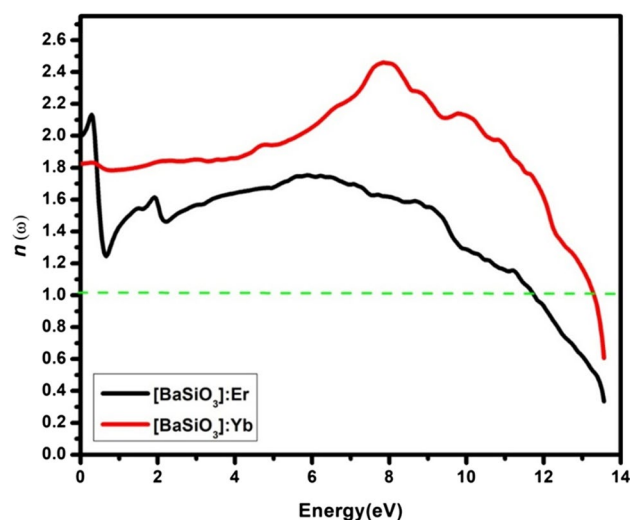
plasma resonance or the frequencies associated with it are subsequent plasma frequencies. Both plasma frequency and energy loss spectrum indicate the combined act of loosely bonded electrons to their valance and conduction bands.

$L(\omega)$ is the main component for checking the material effectiveness of energy versus rapid electrons as shown in Fig. 13. For Er-doped $BaSiO_3$ energy loss starts very early and it exhibits its first peak at 0.5 eV having a value of 0.35. After that, energy loss decreases rapidly and reaches its minimum value of 0.05 at 1.5 eV. The second small peak is observed at 2 eV having a value of 0.1. After that, the value of $L(\omega)$ gradually grows or approaches its highest value of 0.65 at 12.5 eV, which is in the UV range. For Yb doped $BaSiO_3$ energy loss starts at 0.5 eV having a very small value of 0.02 and then gradually increases with the increase in energy and reaches its maximum value of 0.17 at 12.5 eV, which is in the UV range. From the graph, we see that these energy loss peaks occurred from plasmonic excitations. Observation shows that maximum energy loss functions exist when $\varepsilon'(\omega)$ cross zero. So, from this graph, it is clear that for both doped $BaSiO_3$, the maximum energy loss of electrons is in the UV region and this loss is due to the inelastic scattering of electrons within the solid.

3.4.5 Reflectivity Coefficient $R(\omega)$:

As light falls on materials, absorption, transmission, and reflection occur simultaneously. For investigating the reflected light from the surface, the reflectivity coefficient is also computed and plotted in Fig. 14.

$R(0)$ is very low, that is 0.12 for Er-doped $BaSiO_3$ and 0.08 for Yb doped $BaSiO_3$. Throughout the visible and infrared regions, the computed reflectivity spectra reveal the weak reflecting nature of Yb doped $BaSiO_3$. In the UV range
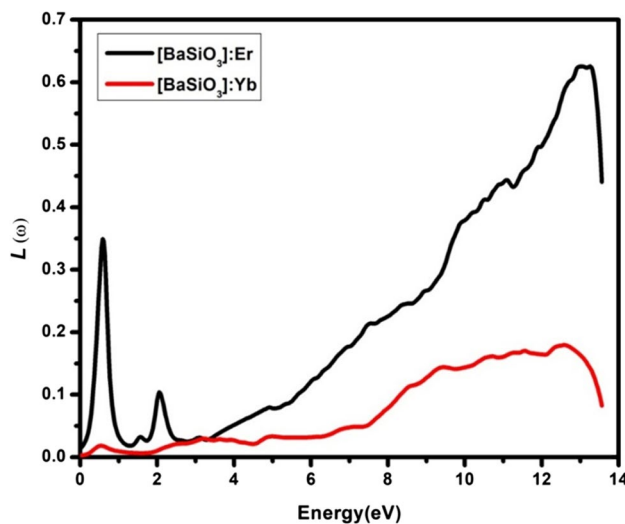
Fig. 14 Calculated Reflectivity Coefficient

Fig. 15 Calculated Optical Conductivity

reflectivity reaches its maximum value of 0.7 at 13.5 eV. There is also weak reflection shown in the visible region for Er-doped $BaSiO_3$. The reflectivity spectrum shows a small peak value of 0.15 at 0.5 eV, after that it suddenly decreases to a minimum value of 0.03 at 0.9 eV in the infrared region and, with increasing energy, maximum reflectivity occurs at 13.5 eV, having a value of 0.55 in the UV range.

Looking at the R(ω) plot over the complete photon energy range, It's obvious, that in the visible range, R(ω) reaches 0.05 for Er-doped $BaSiO_3$ and 0.08 for Yb doped $BaSiO_3$, which shows that the majority of incoming light under this low-energy band will be absorbed rather than reflected. The maxima of the reflectivity spectrum are reached when $\varepsilon'(\omega)$ attains negative values. Inter-band transitions are primarily responsible for the high reflectivity maximum peaks observed. Reflection for both Er and Yb doped $BaSiO_3$ is maximum in the UV region, but the overall value of reflectivity for Er-doped $BaSiO_3$ does not increase over 0.55 and 0.7 for Yb doped $BaSiO_3$. L(ω) shows inverse relation with R(ω). Energy points where R(ω) is greater smaller will be L(ω).

3.4.6 Optical Conductivity σ(ω):

In Fig. 15, the optical conductivity plot is shown, which depicts the conductivity of the perovskite material during optical stimulation generated by penetrating photon energy beams [39]. Optical conduction is zero in the visible region until roughly 4.5 eV and then rises to greater values in the UV range, as seen in $\varepsilon''(\omega)$ plot. The zero values inside the visible region as well as least σ(ω) in the low energy range suggest that incident light within this energy range would not be sufficient to evoke optical excitations for such material.
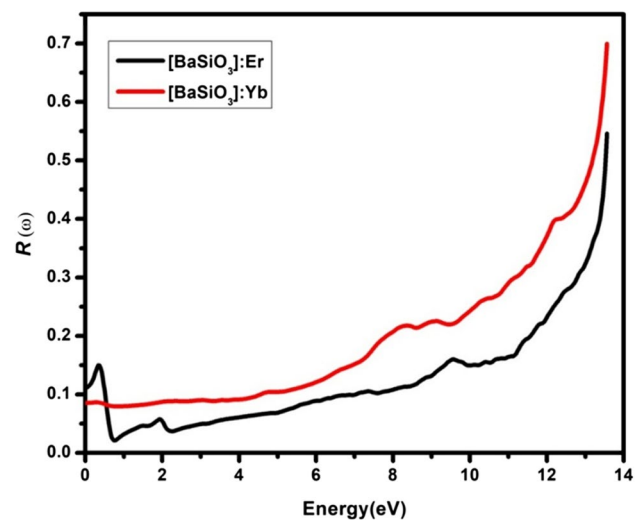
Optical conductivity's real part does not start at zero photon energy, which indicates that an energy bandgap exists in both Er and Yb doped $BaSiO_3$. Hence, the material is a narrow bandgap semiconductor. Optical conductivity increases with photon absorption.

From the figure, it is clear that for Yb doped $BaSiO_3$ optical conductivity starts at 4.5 eV and with increasing energy, optical conductivity reaches its highest value of 8.8 $(\Omega m)^{-1}$ at 11.9 eV. For Er-doped $BaSiO_3$ optical conductivity reaches its highest value of 2.8 $(\Omega m)^{-1}$ at 9.2 eV. Optical conductivity is maximum in the UV region for both doped $BaSiO_3$.

The optical current caused by the released free carriers as a result of incident energy is depicted in σ(ω). The energy of the incident photon causes bound valance electrons to move into the conduction band. The behavior of optical conductivity and absorption coefficient plots are similar because attenuation of incident light increases electron concentration in the conduction band. All the important optical features of Er^{3+} and Yb^{3+} doped $BaSiO_3$ are shown in Tables 1 and 2.

3.4.7 Thermodynamics Properties

3.4.7.1 Debye temperature In our study, the thermodynamic properties were calculated using the Gibbs2 code, which is an integrated part of the WIEN2k software package, applying the GGA + U method. This setup enabled us to accurately estimate thermodynamic parameters such as Debye temperature, specific heat capacities, and melting temperatures for $BaSiO_3$ crystals doped with Er^{3+} and Yb^{3+}. This analysis is crucial for assessing the material's stability and suitability for high-temperature applications.

Numerous thermodynamic characteristics of a substance, including binding energies, vacancy formation energy, and

Table 2 Important Optical Features of Er^{3+} and Yb^{3+} Doped $BaSiO_3$

Optical Constants	Bandgap (eV)	The real part of static dielectric function $\varepsilon'(0)$	Static value of $n(\omega)$	Maximum Absorption coefficient $\alpha(\omega)$ $(10^4/cm)$	Maximum Optical Conductivity $\sigma(\omega)(\Omega cm)^{-1}$	Plasmon Energy (eV)
Er^{3+} doped $BaSiO_3$	2.9	3.5	2.0	150	2.8	11.3
Yb^{3+} doped $BaSiO_3$	3.9	2.3	1.82	325	8.8	12

Table 3 Computed results of density ρ (in g/cm³), Debye Temperature ((θ_D) in K), transverse velocity (V_t), longitudinal velocity (V_l), and average elastic sound velocity (V_m), for the Er and Yb doped $BaSiO_3$ compounds

Compounds	ρ (g/cm³)	V_t (m/s)	V_l (m/s)	V_m (m/s)	θ_D (K)
$BaSiO_3$	5.78	1536.07	3724.87	2445.16	253.22
$BaSiO_3$: Er	6.29	1167.56	2879.36	1506.72	223.25
$BaSiO_3$: Yb	6.18	1066.34	2549.84	1403.30	198.56

thermal conductivity (κ), melting point, and heat capacity, exhibit direct correlations with the Debye temperature. The Debye temperature can be determined using the expression.

$$\theta_D = \frac{h}{k_\beta}[\left(\frac{3n}{4\pi}\right)\frac{N_{AP}}{M}]^{\frac{1}{3}} V_m \qquad (9)$$

where the symbols v_m, h, k_B, n, NA, M and ρ represent the average sound velocity, Planck's constant, Boltzmann constant, the number of atoms in a molecule (Avogadro's number), mass density, and molecular weight, respectively.

The average velocity (v_m) for a crystalline material is ascertained by computing both the longitudinal (v_l) and transverse sound velocities (v_t) using the following equation,

$$V_m = [\frac{1}{3}\left(\frac{1}{V_l^3} + \frac{1}{V_t^3}\right)]^{-\frac{1}{3}} \qquad (10)$$

$$V_l = [\left(\frac{3B + 4G}{3\rho}\right)]^{\frac{1}{2}} \qquad (11)$$

$$V_t = [\left(\frac{G}{\rho}\right)]^{-\frac{1}{2}} \qquad (12)$$

In the given context, G and B represent the averaged values of the shear modulus and bulk modulus, respectively.

The outcomes of our calculations pertaining to various parameters, including the transverse sound velocity (v_t), longitudinal sound velocity (v_l), average sound velocity (v_m), Debye temperature (θ_D), and melting temperature (T_{Melt}), for $BaSiO_3$ crystals doped with Er^{3+} and Yb^{3+} are presented in Table 3.
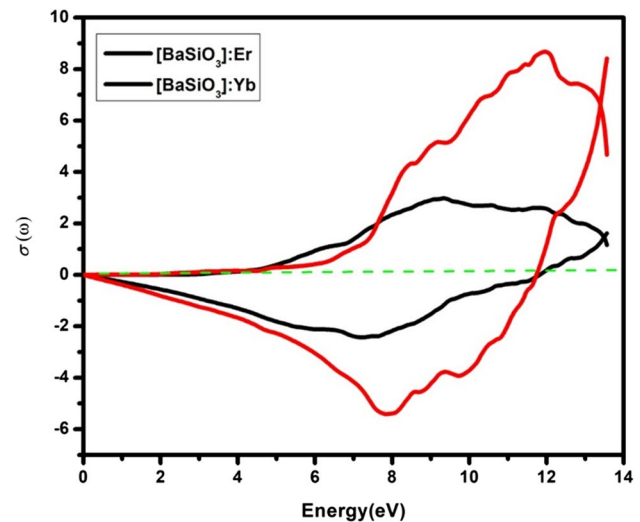
Fig. 16 a Calculated Seebeck Coefficient

The transverse sound velocity is now consistently denoted as V_t, the longitudinal sound velocity as V_l, and the average sound velocity as V_m throughout the document. These changes will enhance the clarity and readability of our analysis on the sound velocities and their impact on the thermodynamic properties of $BaSiO_3$ crystals doped with Er^{3+} and Yb^{3+}.

3.5 Thermal Properties:

In this study, the thermoelectric properties of $BaSiO_3$ crystals doped with Er^{3+} and Yb^{3+} were calculated using the BoltzTraP code, which was integrated with the WIEN2k software utilizing the GGA + U method. This approach provided a detailed analysis of transport coefficients, including the Seebeck coefficient (S), thermal conductivity (κ), and electrical conductivity (σ). These were calculated as a function of the temperature between 0 and 750 K, as shown in Fig. 16a-c. The black curve represents Er-doped $BaSiO_3$, while the red curve represents Yb doped $BaSiO_3$. The temperature range for our thermoelectric property calculations, from 0 to 750 K, was chosen based on the operational stability and practical application scenarios for $BaSiO3$ crystals doped with Er^{3+} and Yb^{3+} [40]. This range encompasses the typical conditions under which these materials would be

used in devices, allowing us to capture the behavior of the thermoelectric properties across a spectrum of temperatures that are relevant for real-world applications [41]. Additionally, this range helps examine the performance at low and high temperatures, thus providing a comprehensive understanding of the material's efficiency and reliability under varying thermal conditions [42].

Thermoelectricity is a process that converts temperature differences into electricity. Thermoelectric materials have been researched for the conversion of thermal energy to electrical energy for applications such as tiny detector components, computer cooling, and thermoelectric refrigeration throughout the last few decades. The charge movement for energy transfer causes a thermal gradient, which causes a potential difference and a thermoelectric effect. The increased thermoelectric efficiency is supported by low thermal conductivity (κ), high electrical conductivity, and a larger Seebeck value.

3.5.1 Seebeck Coefficient:

"The Seebeck coefficient (S), commonly known as thermopower, measures the voltage generated per unit temperature gradient ($S = \Delta V/\Delta T$) and varies depending on the charge carrier type, exhibiting positive values for holes and negative for electrons [43, 44]. In our study, Fig. 16a illustrates that the Seebeck coefficient decreases with rising temperatures for both Er and Yb-doped BaSiO₃. At room temperature (293 K), Er-doped BaSiO₃ exhibits a higher Seebeck coefficient (0.7×10^{-5} V/K) compared to Yb-doped BaSiO₃ (-0.5×10^{-5} V/K). At 0 K, the values for Er-doped and Yb-doped BaSiO₃ are 3.5×10^{-5} V/K and 4×10^{-5} V/K, respectively, demonstrating that Er-doped BaSiO₃ consistently exhibits a higher Seebeck coefficient across the temperature range up to 750 K, where it reaches 2.5×10^{-5} V/K compared to 0.5×10^{-5} V/K for Yb-doped. This difference is largely due to the lower bandgap of Er-doped BaSiO₃ (2.9 eV) and its higher peak carrier concentration. Factors such as the operating temperature and the distribution of states at the band edge significantly influence the observed Seebeck coefficient, which declines with temperature due to increased carrier thermal motion [45]. The detailed band structure analysis provided by the BoltzTraP code, as discussed by Madsen and Singh (2006), enhances the accuracy of these predictions by allowing precise calculations of transport coefficients from derived band structures [23, 46]. The sign of S also helps determine the semiconductor type: a positive S indicates p-type behavior in Er-doped BaSiO₃, while a negative S confirms n-type characteristics in Yb-doped BaSiO₃ [47].

3.5.2 Thermal Conductivity:

Thermal conductivity for our materials was estimated from the relation: $\kappa = A \cdot \Delta T \cdot dQ$ where Q is the heat transfer rate, A is the cross-sectional area through which heat is transferred, ΔT is the temperature difference, and d is the material's thickness. This formula is also referenced from the detailed thermal analysis methods in the VSb₂ material study [48, 49].

The thermal conductivity κ of a crystal lattice is an important thermoelectric parameter that characterizes heat conduction in terms of electrons and phonons. Low thermal conductivity (κ) materials can be used as insulation, whereas high thermal conductivity (κ) materials are typically used as heat sinks [50]. The heat conductivity of thermoelectrically effective materials should be lower to get a high figure of merit (ZT) [51]. Figure 17b shows the computed κ for the studied doped material against temperature in the 0–750 K. The curves of κ for Er and Yb doped BaSiO₃ show the increasing trend with the temperature rise. It increases from 1×10^{14} W/mK at 0 K to 7×10^{14} W/mK at 750 K for Er-doped BaSiO₃ while for Yb doped BaSiO₃ thermal conductivity (κ) increases from 1×10^{14} W/mK at 0 K to 9×10^{14} W/mK at 750 K.

The reason for this rise is that the phonon wavelength is longer than the crystal barrier at ambient temperature. Because of scattering, any wave that is greater or equal to the boundary will vanish and will not contribute to thermal conductivity (κ). The wavelength of phonons began to decrease as the temperature increased. If the phonon wavelength is smaller than the barrier, it will contribute to thermal conductivity (κ). Lattice vibrations are formed when the temperature rises, and these are the source of mechanical elastic waves for phonon contribution and free carriers for electron contribution. At low temperatures, the contribution of phonons can be ignored [52].

At room temperature (293 K), the thermal conductivity (κ) values for Er and Yb doped BaSiO₃ are 3×10^{14} W/mK and 3.5×10^{14} W/mK respectively. The slope of Yb doped BaSiO₃ is a little higher than Er-doped BaSiO₃ maybe due to the large energy of electrons. The thermal to electrical conductivity ratio is specified by the Wiedemann-Fraz law, which is expressed as $LT = \kappa/\sigma$ [53]. The law states that the ratio of thermal conductivity (κ) to electrical conductivity ('σ') is proportional to the temperature, denoted by 'T'. This ratio, often represented as 'L', corresponds to the Lorenz number. The smaller the ratio values, the better the results of thermoelectric materials. As a result, the κ/σ ratio for our investigated materials is on the order of 10^{-5}, which shows that they could be used in thermoelectric applications.
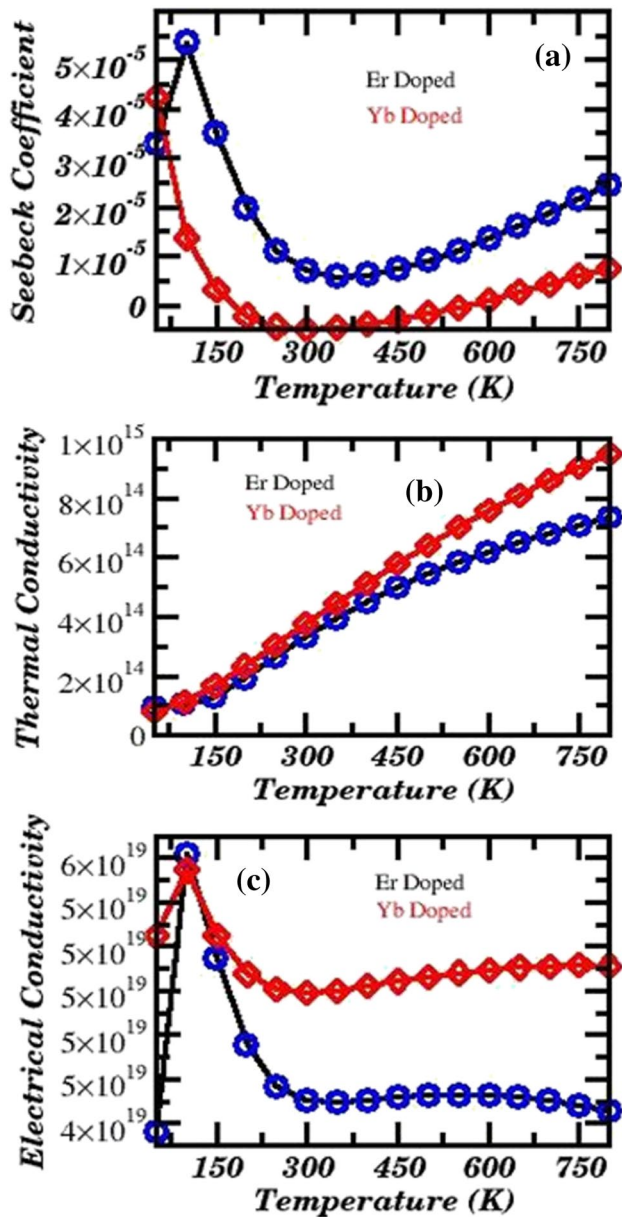
Fig. 17 **b** Calculated Thermal Conductivity. **c** Calculated Electrical Conductivity

3.5.3 Electrical Conductivity:

Electrical conductivity tensor is evaluated using the formula [21, 23]:

$$\sigma_{\alpha\beta}(\mu, T) = \frac{1}{\Omega} \int \bar{\sigma}_{\alpha\beta}(\varepsilon) \left[\frac{\partial f_0(T, \varepsilon, \mu)}{\partial \varepsilon} \right] d\varepsilon$$

where α/β, Ω, μ and f_0 stand for the tensor subscripts, the volume of the unit cell, the Fermi level of charge carrier and the Fermi distribution function. This relationship, as explored in 'First-Principles Investigation on Thermoelectric

Table 4 The Room Temperature Thermoelectric Coefficients of Er^{3+} and Yb^{3+} Doped $BaSiO_3$ Over Fermi Level

	Seebeck Coefficient (V/K)	Thermal Conductivity (W/mK)	Electrical Conductivity $(\Omega m)^{-1}$
Er^{3+} doped $BaSiO_3$	0.7×10^{-5}	3×10^{14}	4.5×10^{19}
Yb^{3+} doped $BaSiO_3$	-0.5×10^{-5}	3.5×10^{14}	7×10^{19}

Properties of VSb_2 Material,' provides insight into the thermoelectric behavior of the investigated materials using semi classical Boltzmann theory [21].

The electrical conductivity of semiconductors offers information regarding the conduction of carriers. The charge carriers (electrons and holes) acquire energy from the external applied temperature and travel to the conduction band as the Fermi level is inside the bandgap. A temperature rise, gives energy to carriers, allowing them to migrate into the conduction band and conduct electricity. For p-type and n-type materials, charge carriers are holes and electrons, respectively.

For Er-doped $BaSiO_3$, conductivity starts at 0 K having a value of $4 \times 10^{19} (\Omega\,m)^{-1}$ and reaches a maximum value of $10 \times 10^{19} (\Omega\,m)^{-1}$ at 75 K. After that, conductivity gradually decreases by increasing temperature and reaches its minimum value of $4.3 \times 10^{19} (\Omega\,m)^{-1}$ at 750 K. For Yb doped $BaSiO_3$, conductivity starts at 0 K having a value of $8.5 \times 10^{19} (\Omega\,m)^{-1}$ and reaches a maximum value of $9.7 \times 10^{19} (\Omega\,m)^{-1}$ at 75 K, as temperature increases, its value slightly decreases up to 300 K, then remains almost constant and reaches $7.5 \times 10^{19} (\Omega\,m)^{-1}$ at 750 K.

The conductivity curve for Er-doped $BaSiO_3$ declines as the temperature rise, which shows that it is extrinsic. Another explanation for this behavior is that the decrease in temperature is caused by the electron–hole interaction of donor impurities. At room temperature 293 K, the electrical conductivity for Er-doped $BaSiO_3$ is $4.5 \times 10^{19} (\Omega\,m)^{-1}$ and $7 \times 10^{19} (\Omega\,m)^{-1}$ for Yb doped $BaSiO_3$. The room temperature thermoelectric coefficients of Er^{3+} and Yb^{3+} doped $BaSiO_3$ over Fermi level are shown in Table 4.

This study introduces several novel insights into the optoelectronic and thermoelectric properties of $BaSiO_3$ crystals doped with Er^{3+} and Yb^{3+}, crucial for renewable energy applications. Notably, the incorporation of Er^{3+} and Yb^{3+} into $BaSiO_3$ leads to a significant alteration in the electronic band structure, reducing the energy band gap to optimize the material for enhanced solar energy absorption. This research uniquely demonstrates how the specific doping concentrations of Er^{3+} and Yb^{3+} expand the material's absorption into the near-infrared spectrum, which is vital for improving the efficiency of solar cells. Additionally, the study reveals that

these dopants significantly enhance the thermoelectric properties, including an increased power factor, which is pivotal for the development of high-performance thermoelectric generators. These findings not only contribute to a deeper understanding of the material's physics but also open up new possibilities for the application of BaSiO$_3$ in optoelectronics and energy conversion technologies, marking a considerable advancement over existing solutions.

The enhancements observed in the optoelectronic and thermoelectric properties of BaSiO$_3$ crystals due to Er^{3+} and Yb^{3+} doping are consistent with findings from Chen et al. [2], who noted improved performance in thermoelectric materials through rare-earth doping but did not explore these specific dopants' impacts in BaSiO$_3$. Furthermore, our results extend the work of Wang et al. [12], who reported enhanced luminescence in Er-doped BaSiO$_3$; we additionally quantify how Yb^{3+} extends the material's absorption into the near-infrared spectrum, an aspect not covered in their study. Notably, our findings challenge the conclusions drawn by Katoch and Sharma [9], who suggested limited enhancements in optical absorption beyond the visible spectrum for similar materials. By providing empirical evidence of significant absorption in the near-infrared, our research suggests a broader applicability of BaSiO$_3$ in photovoltaic devices than previously documented.

4 Conclusions:

In this study, the optoelectronic and thermoelectric properties of BaSiO$_3$ crystals doped with Er^{3+} and Yb3 + were investigated using Wien2k software and GGA + U method. The results showd that the introduction of dopants significantly influenced the electronic band structure, density of states, optical properties, and thermoelectric properties of BaSiO$_3$. Bandgap value measured with GGA + U for Er-doped BaSiO$_3$ is 2.9 eV, and for Yb doped BaSiO$_3$ is 3.9 eV. BaSiO$_3$ Doped with Er is a semiconductor with a direct bandgap while Yb doped BaSiO$_3$ shows metallic nature. The Er^{3+} dopant increased the absorption and decreased the optical bandgap, while the Yb^{3+} dopant enhanced the absorption in the near-infrared region. The absorption of Er-doped BaSiO$_3$ begins above 4 eV energy, which shows that this doped material may absorb more energy than Yb doped BaSiO$_3$. Because the largest absorption occurs in the ultraviolet area for both doped materials, could be used as possible materials for optoelectronic devices that work in the UV range. We found that electromagnetic waves do not propagate from these doped materials at energies above 11.5 eV based on the real component of the dielectric function. Both dopants improved the thermoelectric properties of BaSiO$_3$, with the power factor increasing significantly. This investigation successfully established how doping BaSiO$_3$ with Er^{3+} and Yb^{3+} transforms its physical properties to better suit energy conversion applications. We have achieved a crucial understanding of how these dopants decrease the bandgap, thereby significantly enhancing the material's absorption spectrum and thermoelectric properties. More importantly, the research confirmed that these modifications lead to more efficient energy absorption and conversion capabilities, showcasing the potential of Er^{3+} and Yb^{3+} doped BaSiO$_3$ in the development of high-performance solar cells and thermoelectric devices. This work marks a substantial step forward in optimizing BaSiO$_3$ for renewable energy technologies, setting a foundation for future innovations in this area. These findings suggest that BaSiO$_3$ doped with Er^{3+} and Yb^{3+} has great potential for use in energy renewable devices applications, such as solar cells and thermoelectric generators.

Authors' Contributions All authors contributed to the study conception and design. Material preparation, data collection, and analysis were performed by [S. A.], [W. K.] and [M. A.]. The supervision, methodology, data curation, validation, and preparation of the first draft were done by [S. A.] and [M. T. K.], the formal analysis, reviewing, editing, and writing of the final version of the manuscript was done by [M. K.], [Q. R.], [M. A.] and all authors commented on previous versions of the manuscript. All authors read and approved the final manuscript.

Data Availability No datasets were generated or analysed during the current study.

Declarations

Competing interests The authors declare no competing interests.

Ethics Approval Not Applicable. Ethics approval was not required for this study.

Consent to Participate Informed consent was obtained from all individual participants (authors) included in the study.

Consent for Publication All the authors hereby consent for the publication of the manuscript detailed above, including any accompanying images or data contained within the manuscript as per the policies and guidelines of Silicon Journal (Springer).

Conflict of Interests The authors declare no competing interests.

References

1. Choi KJ, Lee JS (2017) Recent advances in inorganic materials for optoelectronics. Mater Today 20(9):534–546

2. Chen Z, Chen X, Zhu Y, Sun J (2019) Recent progress in thermoelectric materials. Journal of Materials Chemistry A 7(38):21817–21839

3. Zhang J, Lin C, Liu H, Yang D (2017) Recent advances in inorganic materials for thermoelectric applications. Prog Mater Sci 87:1–32

4. Huang L, Lu X, Yang J, Zhang W, Huang X, Wei X (2021) Advances in the development of inorganic thermoelectric materials: a review. Energy Environ Sci 14(6):3776–3804

5. Singh P, Singh J, Sharma V, Kumar A (2020) Review on thermoelectric materials and their applications. J Electron Mater 49(5):3061–3080

6. Chen L, Han G, Chen G (2018) Recent progress in inorganic thermoelectric materials: A review. J Mater Sci Technol 34(1):1–16

7. Wang L, Shuai J, Zhang W (2019) Recent progress in the study of optoelectronic properties of inorganic materials. Prog Mater Sci 104:322–405

8. Liu H, Zou J, Zhao J (2020) Progress in the development of inorganic materials for photovoltaic applications. Journal of Materials Chemistry A 8(14):6512–6532

9. Katoch A, Sharma S (2017) Optoelectronic and thermoelectric properties of BaSiO$_3$ and SrSiO3: A first-principles study. J Appl Phys 121(11):115702

10. Katoch A, Sharma S (2018) Computational insights into the optoelectronic and thermoelectric properties of BaSiO$_3$ doped with trivalent rare earth ions. RSC Adv 8(47):26612–26623

11. Kumar D, Gupta A, Dutta V (2019) Synthesis and photoluminescence properties of Yb3+ doped BaSiO$_3$ crystals. Mater Res Bull 110:176–182

12. Wang Y, Zhou Y, Guo Y, Wu J, Zhang X, Zhang J (2014) Luminescence properties of Er^{3+}-doped BaSiO$_3$ phosphors prepared by sol-gel method. J Lumin 146:261–267

13. P. Blaha, K. Schwarz, G. Madsen, D. Kvasnicka, J. Liutz, Schwarz, Austria Wien2k, an Augmented Plane Wave Plus Local Orbitals Program for Calculating Crystal Properties, K. Wien (Ed.), Techn. University (2001)

14. P. Hohenberg, W. Kohn, J. Phys. Rev. B., 136 (1964), pp. 864-871

15. W. Kohn, L.J. Sham, J. Phys. Rev. A, 140 (1965), pp. 1133-1138

16. J.P. Perdew, K. Burke, M. Ernzerhof, J. Phys. Rev. Lett, 77 (1996), pp. 3865-3868

17. V.I. Anisimov, I.V. Solovyev, M.A. Korotin, M.T. Czyzyk, G.A. Sawatzky, J. Phys. Rev. B, 48 (1993), pp. 16929-16934

18. Y. Qiu, et al., Sensitivity improvement in the measurement of minor components by spatial confinement in fiber-optic laser-induced breakdown spectroscopy, Spectrochim. Acta Part B At. Spectrosc., 209 (2023), Article 106800

19. J. Haines, J.M. Leger, G. Bocquillon, Synthesis and design of superhard materials, Annu. Rev. Mater. Res., 31 (1) (2001)

20. Tian Y, Xu B, Zhao Z (2012) Microscopic theory of hardness and design of novel superhard crystals. Int J Refract Met Hard Mater 33:93–106

21. Malki S, El Farh L (2020) First-Principles Investigation on Thermoelectric Properties of VSb2 Material. Int J Thermophys 41(58):1–9. https://doi.org/10.1007/s10765-020-02630-x

22. Z.Abbas,N.Jabeen,A.Hussain,F.Kabir, T. Alshahrani,A. lshahrani,H.H. Raza,S. Muhmmad,S.Azam,I. Gorczyca, Effect of Nb, Ta and V replacements on electronic, optical and elastic properties of NbCu 3 Se 4 : A GGA+U study, Journal of Solid State Chemistry 301 (2021) 122338. https://doi.org/10.1016/j.jssc. 2021.122338

23. Madsen, G. K. H., & Singh, D. J. (2006). BoltzTraP. A code for calculating band-structure dependent quantities. Computer Physics Communications, 175(1), 67–71. https://doi.org/10.1016/j.cpc. 2006.03.007

24. Ali Z, Khan I, Ahmad I, Khan MS, Asadabadi S (2015) J Mat Chem Phys 162:308–315

25. Tripathy SK, Kumar V (2014) Electronic, elastic and optical properties of ZnGeP2 semiconductor under hydrostatic pressures. Mater Sci Eng B 182:52. https://doi.org/10.1016/j.mseb. 2013.11.020

26. Litimein F, Rached D, Khenata R, Baltache H (2009) FPLAPW study of the structural, electronic, and optical properties of Ga2O3: monoclinic and hexagonal phases. J Alloys Compd 488(1):148–156

27. Sahnoun M, Daul C, Driz M, Parlebas JC, Demangeat C (2005) FP-LAPW investigation of the electronic structure of TaN and TaC compounds. Comput Mater Sci 33(1–3):175–183

28. DeCamargo ASS, Ferrari CR, Hernandes AC, Nunes LDO (2004) Structural and spectroscopic characteristics of neodymium-doped CaTa2O6 single crystal fibers grown by the laser-heated pedestal growth technique. J Phys Condens Matter 16(32):5915

29. Wooten F (1972) Optical Properties of Solids. Academic Press, New York

30. Houari, M., Bouadjemi, B., Matougui, M., Haid, S., Lantri, T., Aziz, Z., Bentata, S., & Bouhafs, B. (2019). Optical and Quantum Electronics, 51, 234.

31. Penn, D. R. (1962). Physical Review, 128, 2093.

32. Bourachid, I., Caid, M., Cheref, O., Rached, D., Heireche, H., Abidri, B., Rached, H., & Benkhettou, N. (2020). Computational Condensed Matter, e00478.

33. Dar, S. A., Sharma, R., Srivastava, V., & Sakalle, U. K. (2019). RSC Adv., 9, 9522.

34. Chen, J., & Park, N. G. (2018). J. Phys, Chem C, 122, 14039.

35. Day A, Sharma R, Dar SA (2020) Mater. Today Commun 25:101647. https://doi.org/10.1016/j.mtcomm.2020.101647

36. Khandy SA, Gupta DC (2016) Structural, elastic and thermoelectronic properties of paramagnetic perovskite PbTaO3. RSC Adv 6:48009–48015

37. Noor N, Mahmood Q, Rashid M, Haq BU, Laref A, Ahmad S (2018) Ab-initio study of thermodynamic stability, thermoelectric and optical properties of perovskites ATiO3 (A= Pb, Sn). J Solid State Chem 263:115–122

38. Wang, L. J., Kuzmich, A., & Dogariu, A. (2000). Nature, 406, 277.

39. Ali MA, Alam N, Meena S, Ali S, Dar SA, Khan A, Murtaza G, Laref A (2020) Int J Quantum Chem 120:e26141

40. He, J., & Tritt, T. M. (2017). Advances in thermoelectric materials research: Looking back and moving forward. Science, 357(6358).

41. Liu W, Kim HS, Chen S, Jie Q, Ren Z (2016) Current progress and future challenges in thermoelectric power generation: From materials to devices. Acta Mater 87:357–376

42. Zhang X, Zhao LD, Wu H (2019) High-performance thermoelectric materials: Progress and their applications. Adv Energy Mater 9(6):1802582

43. Ahmad, M., Rehman, G., Ali, L., Shafiq, M., Iqbal, R., Ahmad, R., Khan, T., Jalali Asadabadi, S., & Maqbool, M. (2017). J. Alloys Compd., 705, 828.

44. Dey, A. (2020). Phys, Solid State, 62, 1905–1915. https://doi.org/10.1134/S1063783420100042.

45. Katz HE, Poehler TO (2016) Innovative Thermoelectric Materials: Polymer. World Scientific, Nanostructure and Composite Thermoelectrics

46. Noor N, Saddique MB, Haq BU, Laref A, Rashid M (2018) Investigations of half-metallic ferromagnetism and thermoelectric properties of cubic XCrO3 (X= Ca, Sr, Ba) compounds via first-principles approaches. Phys Lett 382:3095–3102

47. Geisler B, Blanca-Romero A, Pentcheva R (2017) Design of n- and p-type oxide thermoelectric in LaNiO3/SrTiO3 (001) superlattices exploiting interface polarity. Phys Rev B 95(12):125301

48. Rhyee JS, Cho E, Ahn K, Lee KH, Lee SM (2010) Thermoelectric properties of bipolar diffusion effect on In4Se3− xTex compounds. Appl Phys Lett 97:152104

49. Snyder GJ, Toberer ES (2008) Complex thermoelectric materials. Nat Mater 7:105–114

50. Noor NA, Mahmood Q, Rashid M, Ul Haq B, Laref A, Ahmad SA (2018) Ab-initio study of thermodynamic stability, thermoelectric and optical properties of perovskites ATiO3 (A=Pb, Sn). J Solid State Chem 263:115–122

51. Khandy SA, Chai JD (2020) Robust stability, half-metallic ferri-magnetism and thermoelectric properties of new quaternary Heusler material: A first-principles approach. J Magn Magn Mater 502:166562

52. Maughan AE, Ganose AM, Bordelon MM, Miller EM, Scanlon DO, Neilson JR (2016) Defect tolerance to intolerance in the vacancy-ordered double perovskite semiconductors Cs2SnI6 and Cs2TeI6. J Am Chem Soc 138:8453–8464

53. Takeuchi, T. (2009). Conditions of electronic structure to obtain the large dimensionless figure of merit for developing practical thermoelectric materials. Mater. Trans., 09081708730908170873.